Integrated Resonators in an Ultralow Loss Si_3N_4/SiO_2 Platform for Multifunction Applications

Taran Arthur Huffman, Grant M. Brodnik, Cátia Pinho, Sarat Gundavarapu, Douglas Baney, *Fellow, IEEE*, and Daniel J. Blumenthal, *Fellow, IEEE*

***Abstract*—Integrated optical resonators are key building blocks for an ever-increasing range of applications including optical communications, sensing, and navigation. A challenge to today's photonics integration is realizing circuits and functions that require ultralow loss waveguides on-chip while balancing the waveguide loss with device function and footprint. Incorporating Si_3N_4/SiO_2 waveguides into a photonic circuit requires tradeoffs between waveguide loss, device footprint, and desired device specifications. In this paper, we focus on the design of resonator based circuits in the silicon nitride platform and the balancing of desired properties like quality factor Q, free spectral range, finesse, transmission shape with waveguide design, and footprint. The design, fabrication, and characterization of two resonator-based circuit examples operating at 1550 nm are described in detail. The first design is a thin core, large mode-volume bus-coupled resonator, with a 2.72 GHz free spectral range and a measured intrinsic Q of 60 million and loaded Q on the order of 30 Million, representing the highest reported loaded Q for a large mode volume resonator with a deposited upper cladding. The second circuit is a thicker core, smaller footprint, low loss flat passband third-order resonator filter with an ultrahigh extinction ratio of 80 dB tunable over 100% of the free spectral range and insertion loss under 1.3 dB.**

***Index Terms*—Optical waveguides, optical resonators, high extinction optical filters, resonator filters.**

I. Introduction

INTEGRATED optical resonators have become critical components to an ever-increasing array of applications including data communications [1], microwave photonics [2], and nonlinear optics [3]. The requirements for the resonator's properties vary widely across these functions and applications. For example, frequency stabilization and linewidth narrowing, have substantial demands on the quality factor (Q), while applications like filtering require large free spectral range (FSR), high extinction ratios and engineered passbands. High Q resonators require very low waveguide propagation losses and optimized bus to resonator coupling designs to increase the loaded Q (Q_l) or create a condition of critical coupling. On the other hand, applications like filtering require resonators that can realize tunable higher-order filters with a high extinction ratio, low insertion loss and flat passband. Very high extinction ratio filters using coupled-resonator optical waveguide (CROW) style [4] resonators have achieved extinction ratios as high as 70 dB, using an eleventh-order resonator design [5]. These higher-order resonator filters have application in communications systems [1], parametric amplifiers [6], non-magnetic optical isolators [7], microwave photonics [8], and for quantum communications and computing that employ frequency conversion [9]. Additionally, many of these applications require very high-power handling capabilities either in terms of resonator power storage or linear filter operation.

Reaching very high loaded Q resonators requires very low propagation loss enabled by Si_3N_4 waveguides. Certain applications (e.g., photonic microwave synthesizers and optical gyroscopes) require large mode volumes (FSRs on the order of GHz), single polarization mode operation, and high loaded Q s. These designs utilize thin high-aspect ratio silicon nitride to minimize sidewall scattering and provide a dilute optical mode that can support very high waveguide intensities without inducing optical nonlinearities. This is in contrast to silicon nitride resonators designed for nonlinear optical applications where the light is tightly confined in the core using thick waveguides, with higher propagation loss, and hence smaller mode volumes to reach loaded Q s of similar value [10]. The resonators in this paper are designed for mid- to large mode volumes, and utilize high aspect ratio silicon nitride waveguide designs that have reported propagation losses as low as 0.045 dB/m [11], with the modification that in this work the upper cladding is grown using TEOS-PECVD oxide instead of a bonded thermal oxide upper cladding layer. Waveguides that use bonded hydrogen free thermally grown oxide upper cladding layers have been used to demonstrate resonators with Q_l as high as 42 million [12] with waveguide losses of 0.32 dB/m. However, for flexible, complex photonic circuits and integration with silicon photonic and III/V photonic components, wafer bonded upper claddings pose serious limitations. Therefore, resonators with a deposited upper cladding, such as those demonstrated in this work, enable more

Manuscript received October 24, 2017; revised January 16, 2018 and February 11, 2018; accepted March 6, 2018. Date of publication March 22, 2018; date of current version May 3, 2018. This work was supported in part by Keysight Technologies, the Defense Advanced Research Projects Agency, and Space and Naval Warfare Systems Center Pacific under Contract N66001-16-C-4017 and in part by the Fundação para a Ciência e a Tecnologia under the Ph.D. scholarship PD/BD/105858/2014 and under the Project COMPRESS – PTDC/EEI-TEL/7163/2014. *(Corresponding author: Taran Arthur Huffman.)*

T. A. Huffman, G. M. Brodnik, S. Gundavarapu, and D. J. Blumenthal are with the Department of Electrical and Computer Engineering, University of California, Santa Barbara, Santa Barbara, CA 93106 USA (e-mail: thuffman@umail.ucsb.edu; gbrodnik@umail.ucsb.edu; saratchandra@ucsb.edu; danb@ece.ucsb.edu).

C. Pinho is with the Instituto de Telecomunicações, University of Aveiro, Aveiro 3810-193, Portugal (e-mail: catiap@ua.pt).

D. Baney is with Keysight Technologies, Santa Rosa, CA 95403-1738 USA (e-mail: doug_baney@keysight.com).

Color versions of one or more of the figures in this paper are available online at http://ieeexplore.ieee.org.

Digital Object Identifier 10.1109/JSTQE.2018.2818459

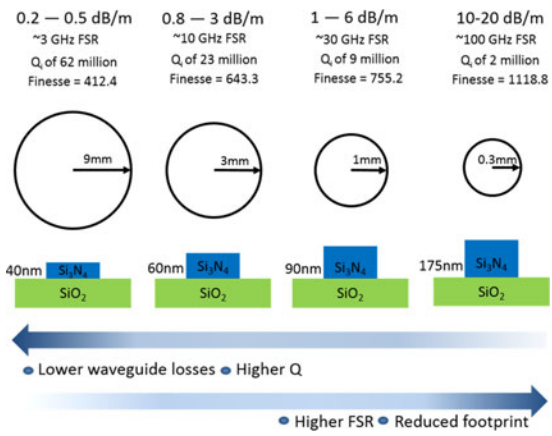

Fig. 1. Typical bend radii and losses are reported for various Si_3N_4 waveguide core thicknesses, as well as corresponding FSR and Q s. The given finesse is for a critically coupled single bus resonator. The loss values reported are from typical measurements, the bend radii are from simulations. The FSR, Q, and finesse are calculated based on the loss and radius for single bus ring at critical coupling. The radii are larger than the bend loss limit, therefore the bending losses are assumed to be negligible.

complex integration with a wide variety of previously demonstrated silicon nitride low loss photonic components such as active layers with hybrid silicon [13] or erbium doped waveguides [14] as well as integration with silicon photonic and III/V photonic circuits.

In this paper, we describe how compact, higher-order bus-coupled resonators circuits can be designed and fabricated on the same platform as large mode volume high Q bus-coupled resonator circuits by tailoring the waveguide geometry to the requirements of a high performance tunable filter or a high performance high Q large mode volume resonator. We present the design and fabrication of a third-order resonator filter, fully tunable over the full FSR, with a record high third-order extinction ratio of 80 dB and an insertion loss of 1.3 dB. We also describe the design and fabrication of a record high mode volume and high loaded Q resonator that operates with a single TE mode, free spectral range and finesse. These circuits are described in the context of the relationship between waveguide geometry and resonator properties, such as FSR, Q and Finesse.

II. Si_3N_4 Waveguide Resonator Design

In the low loss Si_3N_4 waveguide platform, the waveguide losses and the bend-loss-limited radii that can be achieved are dependent on the waveguide core thickness. Higher thickness cores have higher losses from sidewall scattering [15] while thinner cores are limited to extremely large bend radii. This design space is illustrated in Fig. 1 which summarizes waveguide performance and the corresponding resonator characteristics for varying core thicknesses.

The Q of the resonator can be expressed as (1) [12]:

$$Q = (2\pi\nu_0 T_{rt})\, l^{-1} \tag{1}$$

Here, T_{rt} is the round-trip time of the resonator, ν_0 is the free space frequency of light, and l is the fractional power loss per round trip. If the coupling loss is included, then (1) represents the Q_l of the resonator; if the coupling loss is excluded, then it represents the intrinsic Q (Q_i). To reach Q_i values greater than tens or hundreds of millions, extremely low waveguide losses are required. The record lowest loss reported in this platform utilize very thin 40 nm waveguide cores shown at the far left of Fig. 1. Resonators designed using these cores and deposited upper cladding can support Q_is on the order of 62 million, corresponding to a waveguide loss of 0.4 dB/m and a radius of 11.83 mm. However, because the modes of these waveguides are poorly confined, the resonators require bend radii on the order of 10 mm. This bend radius enables large mode volume resonators for device functions and applications that work well with small FSRs and large resonator footprints, such as reference cavities or rotational sensing. The quantities used to calculate the losses and Q factors for the large mode volume resonator on the left and the smaller mode volume resonator on the right in Fig. 1 are described in detail in this paper. The details for second and third resonator examples are based on measured waveguides losses and simulated bend loss performance. The resulting Q, FSR, and finesse are calculated from these values.

Increasing the waveguide core thickness creates a more confined mode and allows much tighter bend radii and FSRs over 100 GHz. The thicker waveguides and their properties are shown at the far right of Fig. 1. Thicker waveguide cores have increased propagation loss and therefore lower achievable Q s. Resonators designed using these cores can support Q_i s on the order of 2 million, corresponding to a waveguide loss of 17 dB/m and a radius of 0.3 mm. Because of this trade-off, these thicker waveguides are better suited to applications in filtering or for devices with specific FSR requirements. Higher-order ring resonators can create extremely high extinction ratios with passbands that have a high shape factor while maintaining low insertion loss even with the higher propagation loss of the thicker waveguides.

Previous high Q resonators published on this platform made use of wafer bonding to create the upper cladding [12]. In this work, we use waveguides with deposited upper claddings, enabling resonator integration with either an erbium doped active layer as in [14] or coupling to a bonded III-V layer as in [13]. Additionally, bonded upper claddings require a very thick SiO_2 layer, usually 15 μm [15], to avoid leakage into the Si layer above the bonded oxide. The bend loss of a given core thickness varies with the upper cladding thickness, shown in the simulation presented in Fig. 2 for a 90 nm waveguide core. The bend loss at low cladding thicknesses is caused by presence of the low index air, which squeezes the mode horizontally. As the cladding increases, this squeezing effect decreases, and the bend loss decreases to an optimum. As the cladding is further increased beyond this optimum, the mode asymptotically approaches the large mode size of the infinite cladding case, and therefore an increasing bend loss. The optimal cladding thickness is substantially thinner than the 15 μm required for a bonded cladding, thus deposited upper claddings can target thicknesses for tighter bend radii. Many devices also require thermal tuning. Using a bonded cladding prevents the application of a metal heater layer as in [16], without the added complexity of substrate removal. Lastly, a bonded cladding creates a visually opaque mask over

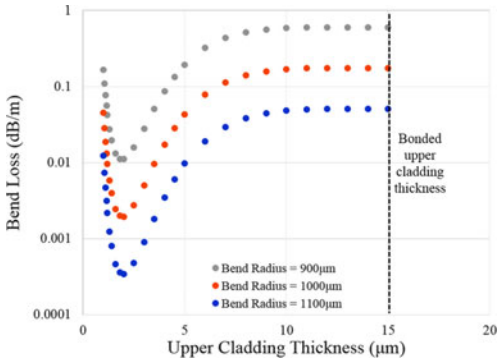

Fig. 2. Simulated bend loss vs upper cladding thickness for three different bend radii for a 90 nm waveguide core at a wavelength of 1550 nm showing an optimum upper cladding thickness for lowest bend limited loss for each bend radii as described in more detail in text.

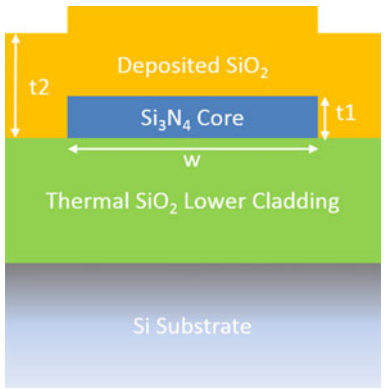

Fig. 3. Schematic of a Si_3N_4 ultra-low loss waveguide. The thickness of the core, t1, can range from 40 nm to 175 nm. The thickness of the cladding, t2, can range from 1 μm to 6 μm. The width of core, w, for a single mode waveguide, varies inversely to the core thickness, ranging from 7 μm for very thin core to 2.2 μm for thicker cores.

the waveguide structures, greatly increasing the difficulty of coupling to the waveguides when testing.

The waveguides are composed of a Si_3N_4 core, clad in SiO_2, as shown in Fig. 3. The lower cladding is 15 μm thermally grown wet oxide on a standard 100 mm Si wafer. The lower cladding is designed to be sufficiently thick to prevent any leakage to the high index Si. Thermal SiO_2 has excellent optical properties and is preferable over deposited SiO_2 for such a thick film. The core is deposited using low pressure chemical vapor deposition (LPCVD), targeting a stochiometric film. LPCVD films offer very high accuracy for layer thickness and good uniformity across the wafer, which is critical for the thinner nitride cores. The core is defined using deep ultraviolet (DUV) lithography and a dry etch. The upper cladding is deposited using plasma enhanced chemical vapor deposition (PECVD) with thicknesses varying from 1 μm to 6 μm, using tetraethoxysilane (TEOS) as a precursor for Si. We chose PECVD for its good step coverage and a high deposition rate as the uniformity and thickness accuracy of LPCVD are not relevant for the thick upper claddings. TEOS based SiO_2 has been used in the lowest loss waveguide results [11] and outperforms silane, in part because of its improved step coverage [17]. It should be noted that the thermal oxide used for the lower cladding is inherently

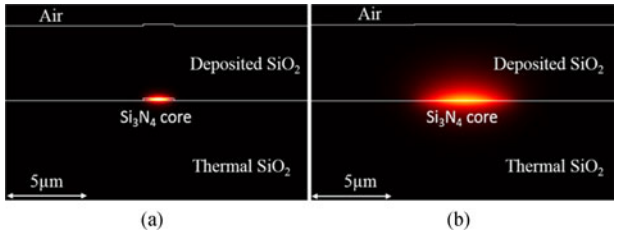

Fig. 4. Waveguide modes for (a) a 175 nm core and (b) a 40 nm core. The waveguide widths are set to the single mode limit.

hydrogen free and therefore the lowest absorption possible due to hydrogen. The thermal oxide also maintains the characteristics of the silicon substrate in terms of roughness which is very small. Deposited films will retain some hydrogen content even after annealing. However, in order to facilitate more complex circuit fabrication and allow control elements like thermal tuning and foundry compatible processes, the TEOS-PECVD reported here represents the lowest loss waveguides with deposited upper cladding to date. This fabrication flow using deposited upper claddings can reliably achieve resonator losses comparable to bonded upper claddings [12].

The waveguide loss is determined by a combination of material losses, scattering losses, and bend losses. The scattering loss is determined by the waveguide mode overlap with the rough interfaces between the core and the cladding. This loss is proportional to the square of the roughness of these interfaces [11]. The interface roughness with the upper and lower surfaces of the core is determined by the deposition techniques and is low, typically $<$0.02 nm RMS [11]. The roughness of the left and right sidewall interfaces is determined by the line edge roughness created by the photoresist and etch, and is on the order of a few nanometers RMS. Thinner cores create modes with low confinement and possess physically smaller sidewalls. The increase in the mode size, and therefore reduced overlap with the rough sidewalls, for a thinner waveguide core is illustrated in Fig. 4. This results in lower scattering loss for thinner cores.

Although these lower confinement cores have improved scattering loss performance, it comes at the cost of the bend radius. Thinner cores experience a higher amount of bend loss at a given radius than thicker cores. This increased bend loss limits the FSR of devices and increases the footprint dramatically, as depicted in Fig. 1. Moreover, because of the high aspect ratio of the waveguides, the TE and TM modes experience extremely different confinement and bend loss characteristics. In the case of a 40 nm waveguide the TE mode has a simulated effective area of 29 μm^2 while the TM mode has an effective area of 61.4 μm^2. As a result, the TM mode requires a much larger bend radius to avoid extremely high losses. In the absence of bends, the TM mode has lower propagation loss, due to reduced scattering from the larger mode size. The radius of the waveguide can be chosen such that the TE mode experiences negligible bend loss, while the TM mode is radiated away. A 40 nm core waveguide bending at a radius of 9 mm has a simulated TE bend loss of 0.001 dB/m whereas the simulated TM bend loss is greater than 1000 dB/m. These waveguides can therefore be used as polarizers and have been demonstrated to have a

TABLE I
WAVEGUIDE AND RESONATOR PROPERTIES

Core Thickness (nm)	Loss (dB/m)	Q_i (millions)	R_{min} (mm)	FSR (GHz)
40	0.5	62.0	9.0	3.23
60	1.2	22.7	3.0	10.70
90	6.0	9.3	1.0	31.60
175	17.0	1.6	0.3	102.70

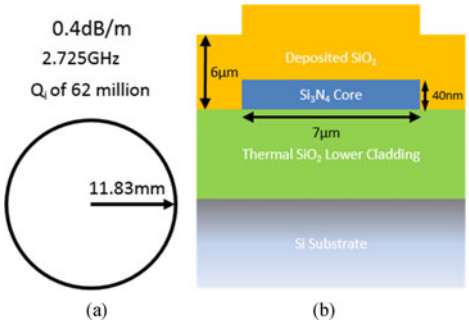

Fig. 5. (a) Resonator characteristics and (b) waveguide geometry.

(measurement limited) polarization extinction ratio as high as 75 dB [18]. Table I summarizes typical loss and radii of different core thickness for the TE mode, as well as the accompanying FSR and Q_i for resonators with those cores.

Table I is constructed from reproducible measured waveguide losses and simulated minimum radii for waveguides with deposited upper claddings and waveguide widths at the multi-mode limit. The Q_i and FSR are calculated assuming a ring made at the minimum radius using the listed loss value. These values can be immediately improved upon by using wider multi-mode waveguides that further reduce the loss and decrease the bend radius [15].

III. LARGE AREA, LARGE MODE VOLUME HIGH Q RESONATORS

High Q resonator performance relies critically on low waveguide propagation losses, making the low loss thin 40 nm core attractive. The large bend limit of the 40 nm core is not a limitation in many applications that benefit from large area and large mode volume resonators. Resonator characteristics for the fabricated high Q device are shown in Fig. 5(a) using the 40 nm waveguide shown in Fig. 5(b). The waveguide width results in a single TE mode, and the TM mode experiences such high loss, that there is no measurable resonance, resulting in a single unique TE mode.

The thin core geometry and accompanying 0.4 dB/m of propagation loss enables Q_l on the order of 30 million and Q_i of 62 million. The resonator layout is shown in Fig. 6. A single bus waveguide was used to maximize the Q_l of the device. The large bend radius of 11.83 mm cannot fit within a single reticle of our DUV stepper, which has dimensions of 21 × 25 mm. We utilize waveguide stitching, demonstrated in [19] with waveguide coils, between multiple reticles to define the entire resonator.

An offset in the bus waveguide is included to minimize unguided light coupling between the input and output fibers.

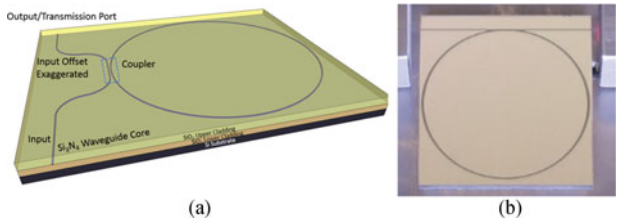

Fig. 6. (a) Single bus high Q resonator layout and (b) image of fabricated resonator.

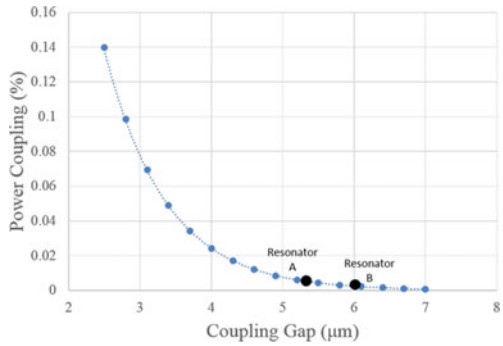

Fig. 7. Coupling simulation for a straight waveguide coupler for a 40 nm core with R = 11.83 mm.

The coupler design is presented in Section A, while the measurement techniques appropriate for characterizing the fabricated high Q resonators and corresponding results are presented in Section B.

A. Coupler Design

To minimize the simulation complexity, the resonator was designed with a directional coupler and straight waveguide bus [12]. The coupling gap between the bus and the resonator waveguide of the directional coupler was determined through simulation using PhoeniX Software's Optodesigner. The modes of the bus and resonator are simulated using film mode matching. The coupling was then calculated using coupled mode theory [21].

The simulation shows an exponential relationship between the gap and the power coupled, shown in Fig. 7. Two different gap values of 5.4 μm and 6.0 μm were fabricated targeting coupling ratios of 0.5% and 0.25% respectively. Resonators with the targeted coupling value of 0.5% are referred to as A, and resonators with the targeted coupling value on 0.25% are referred to as B.

B. Resonator Measurement and Fitting Technique

Several high-Q measurement techniques appropriate for characterization of integrated ring resonators include sideband spectroscopy [22], approaches involving radio frequency (RF) calibrated swept sources, and photonic cavity ring-down [23], [24]. Analog methods involving frequency swept laser sources, such as the piezo tuned laser source used in this work, necessitate an independently calibrated optical frequency standard [25]. The optical transmission of an unbalanced

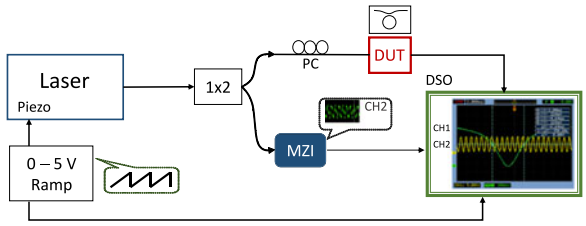

Fig. 8. Calibrated MZI measurement setup. Signal generator (SG) 0–5 V ramp signal to piezo controlled frequency tuning of source laser centered at 1550 nm. The swept optical source is transmitted simultaneously through both the MZI reference and polarization controller (PC) and resonator. Digital sampling oscilloscope (DSO) traces of frequency standard and DUT resonance FWHM are displayed.

Mach-Zehnder interferometer (MZI) is a suitable frequency standard for the high-Q resonator measurements [22] presented. The unbalanced path length of the MZI was chosen such that its FSR is comparable to the full width at half max (FWHM) of the device under test (DUT). We employed a path length difference of 200 xm resulting in an FSR of approximately 1 MHz. However, before implementing the MZI frequency standard, its FSR must be independently determined. For this MZI reference calibration process, an independent SSB swept-source experiment [22], [26] using a discrete stepped-sweep RF frequency synthesizer was conducted. While the discrete nature of the stepped-sweep limited the resolution of an SSB experiment conducted for high Q resonator measurements, it was sufficient for accurately determining the MZI FSR. The calibrated MZI frequency reference enabled analog frequency swept resonance width measurements and greater resolution Q measurements.

For the SSB calibration of the MZI frequency standard, a laser source with carrier at ν_0 was externally modulated by an intensity modulator driven by a microwave frequency synthesizer at frequency f_m. Cascaded fiber Bragg grating filters were used to suppress upper sideband and carrier frequencies, resulting in transmission of only the lower sideband at $\nu_{low} = \nu_0 - f_m$. A linear sweep of the modulation frequency in time generates an RF calibrated optical frequency swept source, $\nu_{low}(t) = \nu_0 - f_m(t)$. Passing the swept source through the unbalanced MZI generates the optical frequency transfer function of the interferometer, with transmitted optical power maxima and minima occurring at integer multiples of the FSR. This calibration method maps a known RF signal to an optical transfer function resulting in a measured FSR of 1.07 MHz.

For resonator measurements, a fiber laser with built-in piezo frequency tuning was transmitted simultaneously through both the MZI and the resonator DUT. A diagram of the complete MZI based Q measurement setup is presented in Fig. 8.

A Lorentzian fit was applied to the resonator Q spectrum to extract key resonator characteristics, specifically the FHWM, power coupling coefficient (κ^2), and ring waveguide loss (α), from the intensity transmission in (2) below [27], [28]. The variable ϕ can be described as the single-pass phase shift, given by the multiplication of the round-trip length with the propagation constant of the circulating mode [27].

$$T = \frac{a^2 - 2ra\cos\phi + r^2}{1 - 2ar\cos\phi + (ra)^2} \tag{2}$$

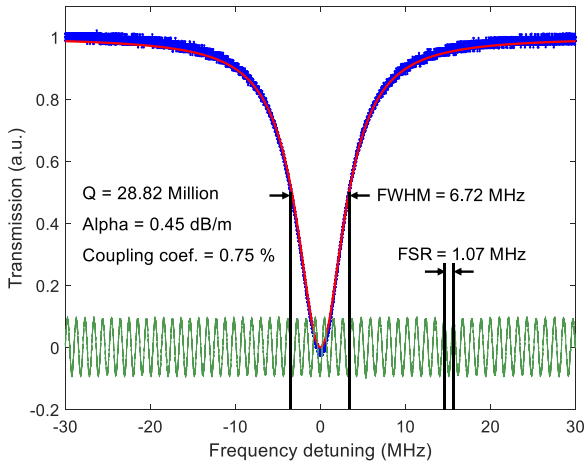

Fig. 9. Resonator measurement with fit.

TABLE II
RESONATOR RESULTS

Sample	Q_l (million)	FHWM (MHz)	Loss (dB/m)	Coup. Coef. (%)	Q_i (million)
A1	21.45	9.02	0.59	1.04	44.32
A2	23.55	8.22	0.42	1.14	61.95
B1	28.10	6.89	0.52	0.68	50.38
B2	28.82	6.72	0.45	0.75	57.59

Parameters a (loss coefficient) and r (transmission coefficient) from (2) are then used to calculate power coupling coefficient, $\kappa^2 = 1 - r^2$, and ring waveguide loss coefficient, $\alpha = -(\log a^2)L^{-1}$.

These measurement techniques were applied to the fabricated resonators described in the previous section. Fig. 9 shows the output port measurement of resonator B2, and remaining resonator results are summarized in Table II. Resonance FWHM values ranging between 7 and 11 MHz were measured, corresponding to loaded Q factors near 30 million.

The loss is consistent across all four devices and the coupling is reproducible across the same coupler design. These resonators were successfully used as stimulated Brillouin scattering lasers detailed in [20]. The Q and loss of these devices are comparable with those reported in the smaller mode volume resonators reported in [12], which uses a wider waveguide, at the cost of an additional TE mode, to reduce its loss a step further [15] and enhance the Q_i to 80 million. The waveguides reported in this work were fabricated with a TEOS-PECVD upper cladding in contrast to the bonded thermal oxide upper cladding used in [15]. The preferred fabrication process of TEOS-PECVD upper cladding represents the best loaded Q high mode volume resonator results to date for a non-bonded upper cladding design.

IV. COUPLED RING COMPACT TUNABLE RESONATOR FILTER

In the previous section, we discussed a large area, high Q resonator based on the 40 nm waveguide core shown in Fig. 1. We next present a tunable resonator filter utilizing the 175 nm waveguide core with a larger FSR and smaller footprint. In a first order ring resonator filter, the extinction ratio of the drop port is

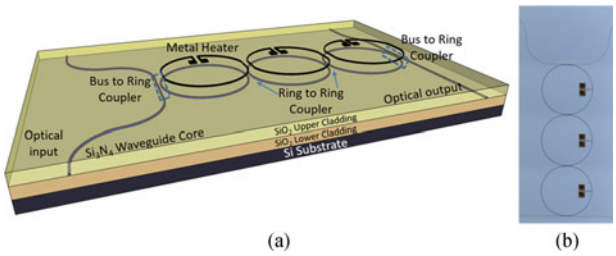

Fig. 10. (a) Third-order ring filter layout and (b) microscope image of fabricated third-order ring filter.

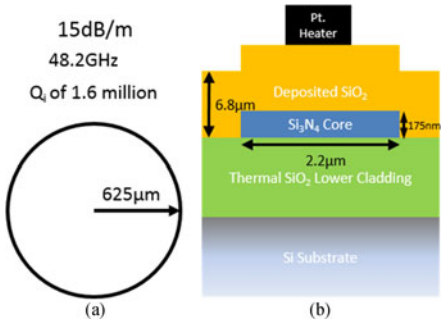

Fig. 11. (a) Resonator characteristics and (b) thermally tunable waveguide composition and geometry.

tied to the width of the resonance peak as well as the insertion loss. High extinction first order filters therefore also have small passbands and higher insertion loss. Increasing the order of the filter allows the passband to be shaped and considerably reduces the insertion loss for a given extinction ratio. Here we report a third order filter, pictured in Fig. 10, with an extinction ratio of 80 dB that is tunable over its entire 48.2 GHz FSR.

The input waveguide has a large offset from the bus coupler to the filter to reduce uncoupled light from the lensed fiber from reaching the resonators, improving the measurement floor. The ring waveguides have a metal (Pt) heater layer on top of the cladding to provide thermal tuning.

The resonator was designed to have a 50 GHz FSR, requiring a waveguide with sufficient confinement to bend at a much tighter radius than the high Q resonator. The resonator characteristics are summarized in Fig. 11(a) using the 175 nm thick waveguide shown in Fig. 11(b). This thickness enables bends tighter than 600 μm for both the TE and TM mode. Initially this waveguide geometry was made using a sputtered upper cladding resulting in very high losses for the TE mode, and the filter was designed to be used with the TM mode. However, the final devices reported here used a PECVD upper cladding and the TE losses decreased to values near the TM mode losses. A discussion of the performance of a hypothetical filter designed for the TE mode is included in the conclusion.

A. Coupler Design

The power coupling coefficients for the bus to ring and ring to ring couplers, κ_1^2 and κ_2^2, have a significant impact on filter performance. To improve the accuracy of the design we calibrated the relationship between waveguide gap and coupling coefficient using fabricated test structures.

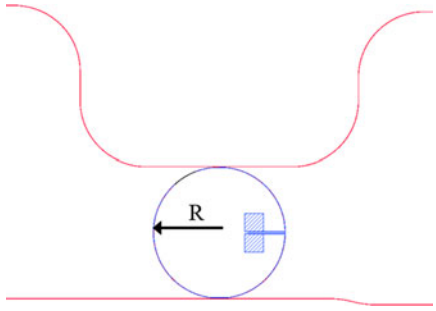

Fig. 12. Thermally tunable single order ring filter test structure. The pink layer is the waveguide layer, while the blue layer is the metal layer.

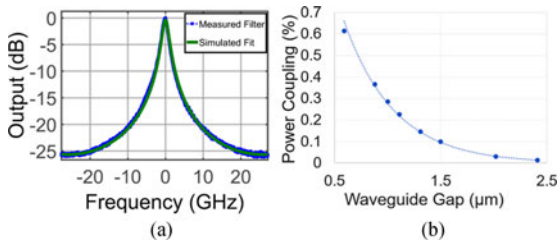

Fig. 13. (a) The analytic fit to a first order ring filter and (b) the measured trend across multiple radii and gaps for the TM mode at a wavelength of 1550 nm.

TABLE III
GAP VALUES WITH CORRESPONDING PREDICTED KAPPA VALUES

Coupler	Gap (µm)	Coupling (κ)
Bus Coupler	1.15	0.13
Ring to Ring Coupler	2.40	0.06

A first-order ring filter test structure, shown in Fig. 12, was used to calibrate the coupling coefficients to the waveguide gap. The drop-port characteristics were measured with a wavelength swept laser into a photodetector. The resulting filter shape was then fit to the equation for the drop port characteristic of a first-order ring in [29] using a least-squares fit, as shown in Fig. 13(a). This yields the relationship between coupling gap and coupling coefficient, shown in Fig. 13(b) for the TM mode.

The ratio between κ_1 and κ_2 was chosen for a target extinction ratio (ER) of 80 dB and a flat passband following [29]. The physical gap values used on the mask, and the corresponding intended coupling coefficients from Fig. 13(b), for the third-order rings are summarized in Table III.

B. Heater Layer and Upper Cladding Thickness

Si_3N_4 waveguides can be thermally tuned [30] using a resistive metal layer on the upper cladding over the core. The heaters are an absorptive metal layer deposited directly over the waveguide requiring careful selection of the upper cladding thickness to balance excess loss from the optical mode overlap with the heater and heater power tuning efficiency. Fig. 14 presents FIMMWAVE simulations of the estimated optical loss as a function of the upper cladding thickness, with loss of the metal layer decreasing exponentially with increased cladding thickness. Modes with upper claddings thicker than 6.5 μm experience negligible loss from the metal layer.

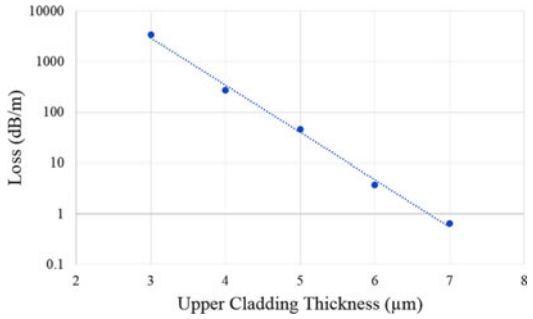

Fig. 14. Metal absorption loss as a function of upper cladding thickness for the TM mode.

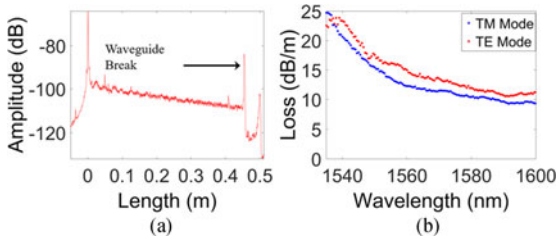

Fig. 15. (a) OBR trace and (b) its resulting loss fit. The trace is for the TM mode. The loss increase at shorter wavelengths is primarily caused by material losses, and is expected to peak at 1520 nm [15].

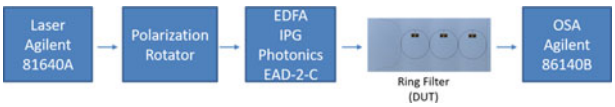

Fig. 16. Schematic representation of measurement setup.

C. Third-Order Ring Filter Characterization

1) Waveguide Characterization: A spiral structure, 0.5 m in length, was fabricated to measure the propagation loss using an optical backscatter reflectometer (OBR) as described in [31]. Fig. 15(a) is a TM polarized OBR trace showing reflected power as a function of propagation distance. Fitting a slope to the trace in Fig. 15(a) yields the waveguide loss, shown in Fig. 15(b) for both TE and TM polarizations. The two different modes have nearly the same propagation loss, with a minimum loss of 9.2 dB/m and 10.5 dB/m at 1590 nm, and a loss of 15.1 dB/m and 17.0 dB/m at a wavelength of 1550 nm.

2) Third-Order Ring Filter Measurement: A wavelength swept laser source was used to measure the passband and to monitor the rings while they were aligned and tuned. However, this approach limits the measurement of the filter stop band to the ER of the laser used. To measure a stopband ER greater than 70 dB, an Agilent 86140B optical spectrum analyzer with sensitivity of −90 dBm used in combination with the tunable laser and erbium-doped fiber amplifier (EDFA) as shown schematically in Fig. 16. Filter tuning and fiber coupling were achieved using a probe setup and precision fiber aligners with the filter maintained at 20 °C using a thermoelectric temperature controllers (TEC) controlled stage.

Each ring within the filter is fabricated with an independently controllable platinum heater. Due to small variations in individual rings within the filter, tuning is required to properly align the resonances as shown in Fig. 17(a) and enables optimization of both the stopband and the passband as shown in Fig. 17(b).

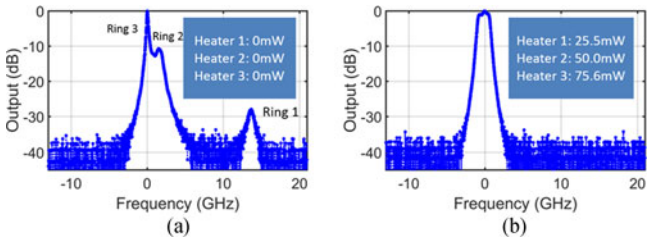

Fig. 17. Optical frequency sweeps of third-order filters at a wavelength of 1550 nm. The measurement is limited by photodetector dynamic range. (a) shows a filter initially out of resonance, (b) shows the same filter tuned to resonance.

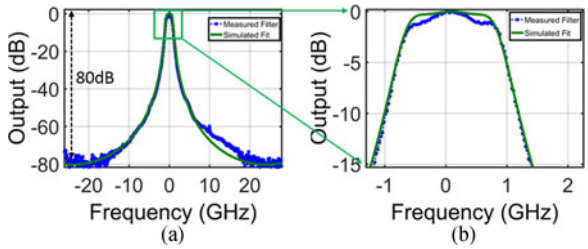

Fig. 18. (a) Third-order filter function at 1550 nm, with an extinction ratio of 80 dB and FSR 48.2 GHz. The analytical fit yields κ_1 fit $= 0.125$, κ_2 fit $=$ 0.005. (b) Third-order filter passband with a shape factor of 0.437 and no ripple.

Filter tuning is achieved through small heater changes as the filter transmission is measured, a technique that has been automated for up to fifth-order filters as reported in [32]. Using this filter alignment technique device yields greater than 90% across a single wafer were achieved.

The optical power transmission of the third-order ring filter is shown in Fig. 18 by plotting the ratio of the input to output filter power. The filter extinction ratio is measured to be 80 dB as shown in Fig. 18(a). Fitting these values to the equation describing the drop port characteristics of a third-order ring in [29] gives coupling values of $\kappa_1 = 0.125$ and $\kappa_2 = 0.05$, close to the targeted values of 0.13 and 0.06 respectively. The filter 3 dB bandwidth and 20 dB bandwidth were measured to be 1.60 GHz and 3.12 GHz respectively. The filter insertion loss was measured using a laser set to the passband of the filter and received by a photodetector. The power measured at the facet was −5.6 dBm, and the power at the detector was −11.7 dBm. Average coupling loss measured on straight waveguide test structures was −2.4 dB. Removing the coupling loss from the power loss in the filter gives an insertion loss of 1.3 dB.

The heaters were used to independently align the rings to realize a third-order filter function. If the power dissipated in the heaters is increased uniformly, such that the differences in power between each heater from the alignment are maintained, the filter can be tuned over its full FSR while maintaining the filter shape. Tuning the rings in this manner results in an efficiency of 0.461 GHz per mW of power per ring, equivalent to 0.105 W/FSR, shown in Fig. 19.

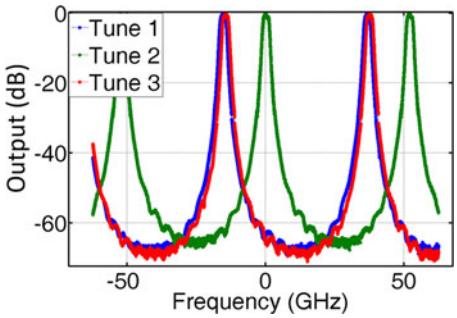

Fig. 19. A third-order ring filter is tuned over its full FSR. Tune 1 represents no thermal tuning, tune 2 represents 50 mW of thermal tuning, and tune 3 represents 110 mW of tuning.

3) Metal Layer Loss Characterization: The spiral test structure does not include a metal layer, and therefore the measurement does not include any loss incurred by the metal layer. To evaluate metal layer induced losses, we compare the losses of two identical first-order rings, one with a metal tuning layer deposited and the other without a metal tuning layer. Fitting the two filter functions to the theoretical model in [29], we find the additional loss of the metal layer to be 1.7 dB/m at 1550 nm.

V. Conclusion

We presented, for the first time, the design and characterization of large mode volume resonators with Q_is as high as 60 million with a unique TE mode. We demonstrated a high yield, wafer-scale fabrication process utilizing a TEOS-PECVD deposited upper cladding compatible with active integration techniques. In contrast to lower loss bonded thermal oxide upper cladding structures, this preferred fabrication process represents the best loaded Q high mode volume resonator results to date. In addition, we demonstrated a third-order filter with a record 80 dB extinction ratio and an insertion loss of 1.3 dB, fully tunable over its FSR of 48.2 GHz.

Several techniques can be employed to further improve the Q of the thin core, large area resonator. The 40 nm high Q resonator, reported here, relies on reduction of waveguide losses to reach higher Q s. Larger widths can substantially reduce the propagation loss of the waveguide to reach higher Q values, but risk introducing an additional TE mode. Preserving single mode operation is essential for several applications, such as rotational sensing [33]–[35]. To improve the waveguide loss, yet preserve a single TE mode, the width of the resonator must be chosen such that the second mode will experience very high bend loss compared to the fundamental mode. Future work includes changing widths to improve the waveguide loss, and therefore the Q, while maintaining a unique TE mode.

The footprint and insertion loss of the 175 nm third-order filter can be improved by utilizing the TE mode rather than the TM mode. The filters demonstrated in this paper used the TM mode of the high aspect ratio Si_3N_4 waveguides, due to initially high TE mode loss. Improved fabrication techniques have reduced the TE mode loss to that of the TM mode. As future work, we will utilize the TE mode to increase the FSR by nearly a factor of two, while reducing the round-trip loss and improving the insertion loss. In addition, the tunability of demonstrated filters can be improved by utilizing alternative tuning techniques as opposed to electrical heaters. This will improve the tuning speed and power efficiency of the filter.

Acknowledgment

The authors would like to thank K. Nelson, J. Nohava, J. Wu, and M. Puckett for useful discussions and guidance on the large mode volume resonator specifications. We also thank B. Stamenic for help in processing samples in the UCSB nanofabrication facility, W. Renninger for help with the measurement techniques for Brillouin gain profiles, and J. Sexton, J. Hunter, and D. Larson at Honeywell for the cladding deposition, precladding preparation, and anneal process. The views and conclusions contained in this paper are those of the authors and should not be interpreted as representing official policies of DARPA, the U.S. Government, or Keysight Technologies.

References

[1] M. A. Popovíc *et al.*, "Multistage high-order microring-resonator add-drop filters." *Opt. Lett.*, vol. 31, no. 17, pp. 2571–2573, 2006.
[2] V. S. Ilchenko and A. B. Matsko, "Optical resonators with whispering-gallery modes—Part II: Applications," *IEEE J. Select. Topics Quantum Electron.*, vol. 12, no. 1, pp. 15–32, Jan./Feb. 2006.
[3] Y. Xuan *et al.*, "High-Q silicon nitride microresonators exhibiting low-power frequency comb initiation," *Optica*, vol. 3, no. 11, pp. 1171–1180, 2016.
[4] A. Yariv, Y. Xu, R. K. Lee, and A. Scherer, "Coupled-resonator optical waveguide: A proposal and analysis," *Opt. Lett.*, vol. 24, no. 11, pp. 711–713, 1999.
[5] B. Little *et al.*, "Tunable bandwidth microring resonator filters," in *Proc. 34th Eur. Conf. Opt. Commun.*, 2008, pp. 1–2.
[6] E. A. Kittlaus, H. Shin, and P. T. Rakich, "Large Brillouin amplification in silicon," *Nature Photon.*, vol. 10, no. 7, pp. 463–467, 2016.
[7] S. Hua, J. Wen, X. Jiang, Q. Hua, L. Jiang, and M. Xiao, "Demonstration of a chip-based optical isolator with parametric amplification," *Nature Commun.*, vol. 7, 2016, Art. no. 13657.
[8] C. G. H. Roeloffzen *et al.*, "Silicon nitride microwave photonic circuits," *Opt. Express*, vol. 21, no. 19, pp. 22937–22961, 2013.
[9] J. W. Silverstone *et al.*, "On-chip quantum interference between silicon photon-pair sources," *Nature Photon.*, vol. 8, no. 2, pp. 104–108, 2014.
[10] X. Ji *et al.*, "Ultra-low-loss on-chip resonators with sub-milliwatt parametric oscillation threshold," *Optica*, vol. 4, no. 6, pp. 619–624, 2017.
[11] J. F. Bauters *et al.*, "Planar waveguides with less than 0.1 dB/m propagation loss fabricated with wafer bonding," *Opt. Express*, vol. 19, no. 24, pp. 24090–24101, 2011.
[12] D. T. Spencer, J. F. Bauters, M. J. R. Heck, and J. E. Bowers, "Integrated waveguide coupled Si_3N_4 resonators in the ultrahigh-Q regime," *Optica*, vol. 1, no. 3, pp. 153–157, 2014.
[13] M. Piels, J. F. Bauters, M. L. Davenport, M. J. R. Heck, and J. E. Bowers, "Low-loss silicon nitride AWG demultiplexer heterogeneously integrated with hybrid III–V/silicon photodetectors," *J. Lightwave Technol.*, vol. 32, no. 4, pp. 817–823, Feb. 2014.
[14] M. Belt and D. J. Blumenthal, "Erbium-doped waveguide DBR and DFB laser arrays integrated within an ultra-low-loss Si_3N_4 platform," *Opt. Express*, vol. 22, no. 9, pp. 10655–10660, 2014.
[15] J. F. Bauters *et al.*, "Ultra-low-loss high-aspect-ratio Si_3N_4 waveguides," *Opt. Express*, vol. 19, no. 4, pp. 3163–3174, 2011.
[16] R. L. Moreira *et al.*, "Integrated ultra-low-loss 4-bit tunable delay for broadband phased array antenna applications," *IEEE Photon. Technol. Lett.*, vol. 25, no. 12, pp. 1165–1168, Jun. 2013.
[17] D. Guan, A. R. Bruccoleri, R. K. Heilmann, and M. L. Schattenburg, "Stress control of plasma enhanced chemical vapor deposited silicon oxide film from tetraethoxysilane," *J. Micromech. Microeng.*, vol. 24, no. 2, 2013, Art. no. 027001.
[18] J. F. Bauters, M. J. R. Heck, D. Dai, J. S. Barton, D. J. Blumenthal, and J. E. Bowers, "Ultralow-loss planar Si_3N_4 waveguide polarizers," *IEEE Photon. J.*, vol. 5, no. 1, Feb. 2013, Art. no. 6600207.

[19] T. Huffman, M. Davenport, M. Belt, J. E. Bowers, and D. J. Blumenthal, "Ultra-low loss stitching for large-area waveguide based delay-line gyroscopes," in *Proc. IEEE Photon. Conf.*, 2016, pp. 478–479.
[20] S. Gundavarapu *et al.*, "Integrated waveguide Brillouin laser," arXiv: 1709.04512 [physics.optics].
[21] R. Stoffer, K. R. Hiremath, M. Hammer, L. Prkna, and J. Čtyroký, "Cylindrical integrated optical microresonators: Modeling by 3-D vectorial coupled mode theory," *Opt. Commun.*, vol. 256, no. 1, pp. 46–67, 2005.
[22] J. Li, H. Lee, K. Y. Yang, and K. J. Vahala, "Sideband spectroscopy and dispersion measurement in microcavities," *Opt. Express*, vol. 20, no. 24, pp. 26337–26344, 2012.
[23] Y. Xuan *et al.*, "High-Q silicon nitride microresonators exhibiting low-power frequency comb initiation," *Optica*, vol. 3, no. 11, pp. 1171–1180, 2016.
[24] D. K. Armani, T. J. Kippenberg, S. M. Spillane, and K. J. Vahala, "Ultra-high-Q toroid microcavity on a chip," *Nature*, vol. 421, no. 6926, pp. 925–928, 2003.
[25] K. Y. Yang, D. Y. Oh, S. H. Lee, Q.-F. Yang, X. Yi, and K. Vahala, "Integrated ultra-high-Q optical resonator," arXiv:1702.05076v2 [physics.optics].
[26] T. Wei, J. Huang, X. Lan, Q. Han, and H. Xiao, "Optical fiber sensor based on a radio frequency Mach–Zehnder interferometer," *Opt. Lett.*, vol. 37, no. 4, pp. 647–649, 2012.
[27] W. Bogaerts *et al.*, "Silicon microring resonators," *Laser Photon. Rev.*, vol. 6, no. 1, pp. 47–73, 2012.
[28] F. Xia, L. Sekaric, and Y. A. Vlasov, "Mode conversion losses in SOI photonic wire based racetrack resonators," in *Proc. 2006 Conf. Lasers Electro-Optics and 2006 Quantum Electron. Laser Sci. Conf.*, 2006, pp. 1–2.
[29] C. Chaichuay, P. P. Yupapin, and P. Saeung, "The serially coupled multiple ring resonator filters and Vernier effect," *Optica Appl.*, vol. 39, no. 1, pp. 175–194, 2009.
[30] R. Amatya *et al.*, "Low power thermal tuning of second-order microring resonators," in *Proc. Conf. Lasers Electro-Optics*, 2007, pp. 1–2.
[31] J. F. Bauters *et al.*, "Ultra-low-loss high-aspect-ratio Si_3N_4 waveguides," *Opt. Express*, vol. 19, no. 4, pp. 3163–3174, 2011.
[32] J. C. C. Mak, W. D. Sacher, T. Xue, J. C. Mikkelsen, Z. Yong, and J. K. S. Poon, "Automatic resonance alignment of high-order microring filters," *IEEE J. Quantum Electron.*, vol. 51, no. 11, Nov. 2015, Art. no. 0600411.
[33] J. Li, M.-G. Suh, and K. Vahala, "Microresonator Brillouin gyroscope," *Optica*, vol. 4, no. 3, pp. 346–348, 2017.
[34] G. A. Sanders *et al.*, "Development of compact resonator fiber optic gyroscopes," in *Proc. IEEE Int. Symp. Inertial Sensors Syst.*, 2017, pp. 168–170.
[35] S. Gundavarapu, T. Huffman, M. Belt, R. Moreira, J. Bowers, and D. Blumenthal, "Integrated ultra-low-loss silicon nitride waveguide coil for optical gyroscopes," in *Proc. Opt. Fiber Commun. Conf.*, 2016, pp. 1–3.

Taran Arthur Huffman received the B.S. degree in physics from the University of Southern California, Los Angeles, CA, USA. He is currently working toward the Ph.D. degree at the University of California, Santa Barbara (UCSB), Santa Barbara, CA, USA.

Since 2012, he has been working as a Graduate Student Researcher at UCSB. His research interests include the design and fabrication of low loss waveguides on the Si_3N_4 platform. Much of his work involves resonators, but he is also developing a method for vertically integrating waveguide layers.

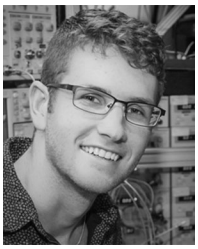

Grant M. Brodnik received the B.S. degree in optical engineering from Rose-Hulman Institute of Technology, Terre Haute, IN, USA, and the M.S. dual-degree from Rose-Hulman Institute of Technology and Seoul National University of Science and Technology, Seoul, South Korea, in 2014 and 2016, respectively. He is currently working toward the Ph.D. degree at the University of California, Santa Barbara, Santa Barbara, CA, USA in electrical and computer engineering with a focus on electronics and photonics, as part of the Optical Communications and Photonic Integration group. While at Rose-Hulman Institute of Technology, He received the Grant for conducting research that involves high-power diode laser characterization and performance metrics.

Cátia Pinho received the Bachelor's degree in physics engineering and the Master's degree in biomedical engineering from the University of Aveiro, Aveiro, Portugal. She is currently working toward the Ph.D. degree at the MAP-tele Doctoral Programme in Telecommunications, University of Aveiro, Aveiro, Portugal. She is currently a Researcher in the Optical Communications and Photonic Integration group, University of California, Santa Barbara, Santa Barbara, CA, USA. Her research interests include optical communications (e.g., photonic integrated circuits, fiber optics, and optical systems testing), biomedicalt signal processing, and development of health information technologies.

Sarat Gundavarapu received the Bachelor's degree in electronics and communication engineering from Jawaharlal Nehru Technological University, Hyderabad, India, in 2007. He is currently working toward the Ph.D. degree in electrical engineering at the University of California, Santa Barbara, Santa Barbara, CA, USA. His research interests include silicon nitride photonics and optical sensors.

Douglas Baney (F'11) received the B.S. degree in electrical engineering from Cal Poly, San Luis Obispo, CA, USA, the M.S. degree in electrical engineering from the University of California, Santa Barbara, Santa Barbara, CA, USA, and the Ph.D. degree from Télécom ParisTech, Paris, France. He has been in the field of microwaves and photonics for the past 35 years. He worked as an R&D Millimeter Wave Engineer in Signal Analysis Division, Hewlett-Packard, and later transferred to HP Laboratories, then Agilent Laboratories, and now Keysight Laboratories where he conducted research in the areas of optical amplifier gain, optical noise figure, and spectral-hole burning and upconversion ZBLAN fiber lasers. Many of the optical amplifier test methods he developed are in use globally for production test of optical amplifiers. Other research he performed or directed includes Faraday-effect optical devices, optical reflectometry, optical coherent reception, and advanced modulation format optical constellation measurement. He was the Leader of the research team that developed the first high-volume commercial laser-based mouse. He is currently a Department Manager in Keysight Labs, where he is responsible for research in microwave test, nonlinear microwave modeling, nanomeasurement, measurement automation, photonics measurement, and integrated photonics applications. He served as General Cochair of OFC, General Cochair of OAA, OSA OFC Budget Committee, Tyndall Award Committee, and has been a member of the IEEE since 1990.

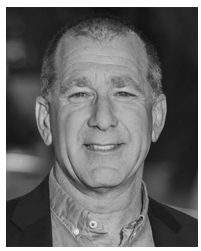

Daniel J. Blumenthal (F'03) received the Ph.D. degree from the University of Colorado—Boulder, Boulder, CO, USA. He is currently a Professor in the Department of Electrical and Computer Engineering, University of California, Santa Barbara (UCSB), Santa Barbara, CA, USA and the Director of the Terabit Optical Ethernet Center, UCSB, and the Head of the Optical Communications and Photonics Integration group, UCSB (www.ocpi.ece.ucsb.edu). He is the Cofounder of Packet Photonics and Calient Networks. He holds 22 patents, has authored and coauthored more than 410 papers, and is the coauthor of *Tunable Laser Diodes and Related Optical Sources* (Wiley-IEEE Press, 2005). His research interests include the areas of optical communications, optical networks and packet switching, optical gyrosensors, photonic integration in InP and ultralow loss waveguides and platforms, and photonic molecule and nanophotonic device technologies. He is the recipient of the Presidential Early Career Award for Scientists and Engineers, the National Science Foundation Young Investigator Award, and the Office of Naval Research Young Investigator Program Award. He has served on the Board of Directors for National LambdaRail and was an Elected Member of the Internet2 Architecture Advisory Council. He is a 2017 Fellow of the National Academy of Inventors, Fellow of the Optical Society of America, and a member of the IEEE since 1990.